Determination of flow using half Fourier echo-planar MR imaging

A.O. Rodríguez-González
Departamento de Ingeniería Eléctrica, Universidad Autónoma Metropolitana-Iztapalapa
09340 México, D.F., Mexico.
e-mail: arog@xanum.uam.mx

Recibido el 15 de octubre de 1999; aceptado el 13 de enero de 2000

Since NMR was first discovered there has been a great interest to study flow with this non-invasive technique. However, the only real-time MR imaging scheme is still EPI (Echo-Planar Imaging). A flow encoded version of Echo-Planar Imaging which employs a Half Fourier method to scan the *k*-space is described and then applied to measure flow in vitro. A water phantom consisting of a pipe with an inner diameter of 2 cm was used to carry out the flow experiments. Details of the velocity measurement technique are outlined and quantitative results are presented. 2D flow maps are also shown.

Keywords: Magnetic resonance imaging; flow determination; echo-planar imaging

Desde el descubrimiento de la RMN ha existido un gran interés en estudiar el flujo con esta técnica no destructiva. Sin embargo, la única técnica imagenológica de resonancia magnética en tiempo real es hasta el momento la imagenología eco planar (Echo-Planar Imaging). En este trabajo describimos una técnica sensible al flujo que emplea un método parcial de Fourier para cubrir el espacio *k*, que posteriormente se aplica para medir flujo en vitro. Para realizar los experimentos de medición del flujo empleamos una manguera de 2 cm de diámetro. Se muestran los detalles de la técnica de medición de velocidad, además de los resultados cuantitativos. Mapas bidimensionales de flujo también se exhiben.

Descriptores: Imagenología por resonancia magnética; determinación de flujo; imagenología eco planar

PACS: 87.61.Cd; 87.61.Ff; 87.61.Lh

1. Introduction

Flow quantification by NMR dates back to 1946, when it was discovered by Bloch [1–5] and Purcell [6–8], who quickly realized the potential of this technique to study flow [9]. The principles of magnetic resonance flow imaging were, first developed by E.L. Hahn [10] and G. Suryan [11] in 1950 and 1951, respectively. These techniques are categorized as phase shift methods and time-of-flight effect modalities.

Suryan demonstrated that water flowing through a MR probe will experience a signal-enhancing effect. This is due to the apparent T_1 of flowing water appearing different from that of stationary water. This effect was observed as a relative increase in signal magnitude resulting from the in-flow of fresh, non-saturated, magnetization into the imaging region. This is the so-called in-flow or spin-refreshment effect. Hahn's spin echo method describes the manner of measuring flow by applying a gradient to yield a phase shift of the signal from moving spins. This phase of the moving spin is linearly proportional to the velocity.

Generally, MR flow imaging modalities are based on either the change of position of the magnetization which happens when the spins move, or the change in the phase of the transverse component of the magnetization, induced by the presence of a magnetic field gradient along the flow direction. A number of reviews of NMR and flow have been published elsewhere [12–21].

The most important characteristic of MR flow imaging is its non-invasive property. It is also capable of discriminating between flowing and motionless spins, permitting formation of an image of flowing material in the presence of static material of the same type. Singer [18, 22–24] employed these ideas to measure the flow of body fluids. He obtained both flow and non-flow images so he could create a procedure to separate out flow from solid tissue.

Flow imaging by NMR is limited to measuring average flow properties over time, in contrast to ultrasound methods [25–33], laser Doppler method [34], capacitance tomography [35] and electrical impedance tomography [36], which measure instantaneous velocities. MRI flow methods are more suitable when the average behaviour is constant or changes slowly compared to the time scale of the NMR experiment. It is particularly important to our study to focus on the laminar flow in which average velocity is constant. Blood flow in the large arteries is an example of this type of flow [37–52]. The dispersion of the tagged spins can make the generation of quantitative data difficult. Time-of flight effects are further constrained by the geometry of the vessel and are more noticeable in straight vessels than curved ones. These techniques are appropriate for quantifying relative velocity and direction. Pelc's review [17] contains relevant references on this matter. Axel [53] and Bradley [19] have also reviewed these techniques. The second type of flow effect rises from the phase shift in the transverse magnetization. This variation of the phase is produced when a magnetic field gradient is applied to a moving fluid. In this case, it is presumed that fluid in each pixel has a single well-defined velocity. Roughly, these imaging methods can be divided into two

groups: phase mapping methods which measure the signal phase directly [54, 55], and Fourier flow procedures which need a number of encoding steps to separate the different velocities in a particular site [56, 57]. An important inconvenience of the Fourier methods is that the flow magnitude is averaged over the acquisition time which may be as long as 5 minutes, so any short time change in flow can not be detected. Firmin and co-workers and others [58–60] have studied in detail the benefits and limitations of these imaging approaches. To assess flow over a very short period of time, for example, in magnetic resonance angiography, fast flow measurement techniques have been developed [61–121].

Firmin *et al.* [122], Debatin and co-workers [123] and Mansfield's group at The University of Nottingham, Britain [70, 77, 124, 125], have demonstrated EPI's validity for velocity mapping. Cine and phase contrast techniques have been introduced. In one method, two images are acquired using two flow-encoding gradients of equal strength but opposite polarity. Static spins are removed by calculating the phase difference, then only the moving spin phase is obtained [17, 19, 53].

2. Flow imaging with half fourier echo-planar imaging

2.1. Echo-planar imaging

Echo Planar Imaging (EPI) was introduced by Peter Mansfield in 1976 [126–128] and is a true snapshot technique which enables the formation of a complete image in 30–100 ms. The rapid nature of this technique is due to the fact that only one RF excitation is needed per image. It thus allows the acquisition of a two-dimensional image from only one Free Induction Decay (FID).

Following the excitation of a slice, the signal is sampled under the influence of two orthogonal gradients (Fig. 1). A gradient G_x (x-axis) is modulated rapidly to generate a series of gradient echoes. This forms the frequency encoding part of the experiment. In conjunction with G_x, another gradient G_y (y-axis) is applied: this gradient is either blipped or continuous and performs the phase encoding part of the experiment. This combination of gradients serves to encode each point in the image with a different degree of phase evolution between echoes and frequency during an echo. A train of phase encoded echoes is thus acquired. After some data manipulation required because of the effect of evolution of sequential echoes under positive and negative read-out gradient lobes, it is possible to apply a 2D-FT (Bidimensional Fourier Transform) to create an image. Generation of a 128×128 image requires the production of 128 gradient echoes with each echo being sampled using 128 data points.

EPI has undergone many modifications since its introduction in 1976 [127]. The original forms of EPI were called Double Echo Planar Imaging (DEPI) and Fast Low Angle Excitation Echo Planar Technique (FLEET) [130], see Fig. 1a. DEPI is a two shot experiment with G_y having positive and

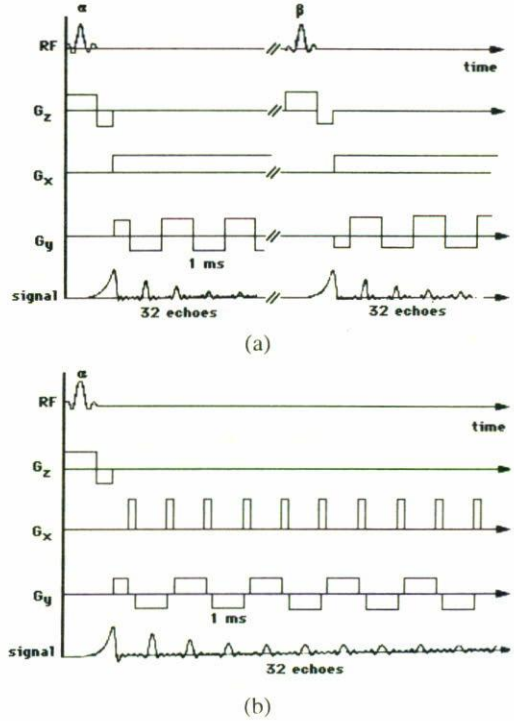

FIGURE 1. (a) Fast low-angle excitation echo-planar technique (FLEET): total data acquisition time = 64 ms, frame repetition rate of up to 10 frames/s (b) Blipped echo-planar single-pulse technique (BEST): total data acquisition time = 32 ms, frame repetition rate of up to 20 frames/s.

negative starting phase in alternate shots. The data sets are corrected by splicing together all the echoes formed in totally positive and totally negative gradients. Two images are produced, which can be re-registered and added to yield a improvement in SNR. Flip angles of 45° and 90° were used to minimize the acquisition time. These techniques originally used a constant phase encoding gradient.

Ljunggren [131] first proposed replacing the continuous phase encoding gradient by a blipped gradient: G_y blips are applied in the spaces between echoes. The resulting trajectory through k-space is a square raster scan. Correction of the time evolution can be achieved by simply reversing the data which makes up every alternate echo prior to Fourier Transform (FT). The scan still starts at the k-space origin and zero filling is still required. This single shot technique is called Blipped Echo Planar Imaging (BEPI) or Blipped Echo Planar Single pulse Technique (BEST) [132, 133], Fig. 1b. BEST is susceptible to the effect of magnetic field inhomogeneities which cause phase errors. Therefore, it is important to ensure that the transverse magnetization is completely in phase at the start of the experiment. This implies the use of a 180° pulse which will be applied immediately following slice selection. Data acquisition begins at the point of maximum signal, when the magnetization is completely refocused.

The modulus version of this experiment, called MBEST [134], is found to be essentially identical to BEST, except for the addition of a large negative G_y gradient pulse

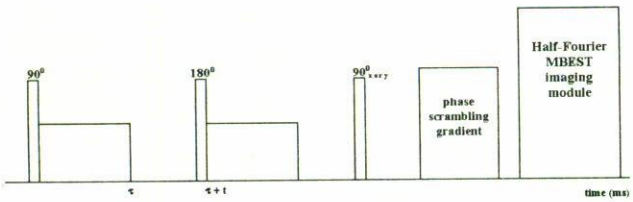

FIGURE 2. Time diagram of flow encoded Half-Fourier Echo-Planar Imaging.

prior to data acquisition. k-space is fully scanned and the FT data produces a modulus image which is considerably more robust and less susceptible to phase errors. The MBEST timing diagram is shown in Fig. 2. EPI is a compact technique which is easily adaptable as an imaging module applied after any suitable spin preparation experiment, such as Inversion Recovery [135] and Spin Echo EPI [136].

Basic references describing the foundations of the principles of MRI abound, so for a fuller description, the reader is referred to the original and review papers [126–129, 136–144] and many well known textbooks [145–158].

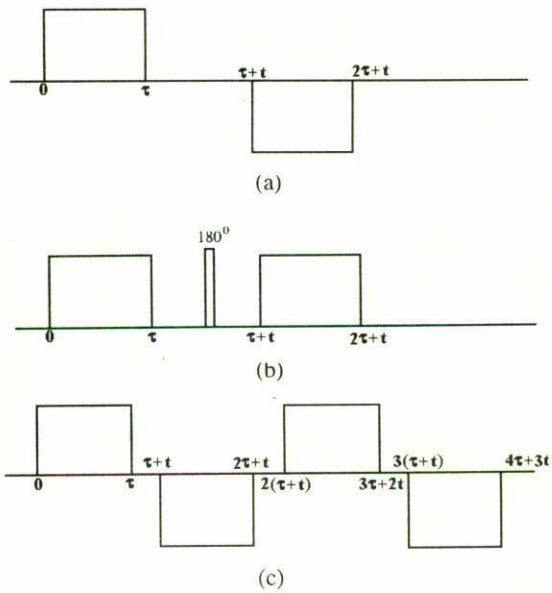

FIGURE 3. Two equivalent flow encoding sequences, which induce a phase shift proportional to the spin velocity; a) simple bipolar gradient, b) a unipolar sequence which uses a 180° RF pulse to refocus the moving spins, c) the even-echo rephasing phenomen.

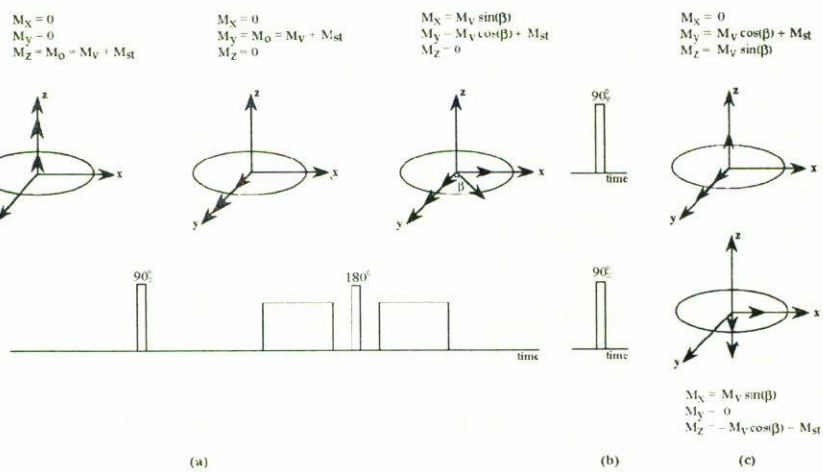

FIGURE 4. Time diagram for the RF pulses, a) flow encoding gradient and graphical description of the position of the magnetization $M(M_x, M_y, M_z)$ when applying the flow encoding sequence, b) the magnetization is flipped with a 90^0 RF pulse applied either along the x or y axis, c) the final position of the magnetization which represents either cosine or sine component.

2.2. Flow encoding gradients

Moran [159] introduced the use of bipolar flow encoding gradients, based on Stejskal and Tanner's sequence [160] to encode flow information via the phase of the NMR signal. The phase generated in such a fashion is proportional to the flow velocity. After application of a bipolar gradient, such as the one shown in Fig. 3, the phase shift induced by flow can be expressed [70, 77],

$$\beta = \gamma G_x v(\tau^2 + \tau t), \qquad (1)$$

where G_x is the strength and t is the duration of the gradient pulses, τ is the delay time between the lobes. The phase is completely independent of the spin position and the phase variation is directly proportional to the spin velocity. An equivalent technique is shown in Fig. 4.

The echo height is reduced by T_2 and decay in the bipolar case and by T_2 decay alone in the case where a 180° pulse is used, so the flow encoding sequence must last for a time less than the spin-spin relaxation time. A schematic description of the sequence is given in Fig. 4. Another important phenomenon occurs when more gradient pulses are applied as

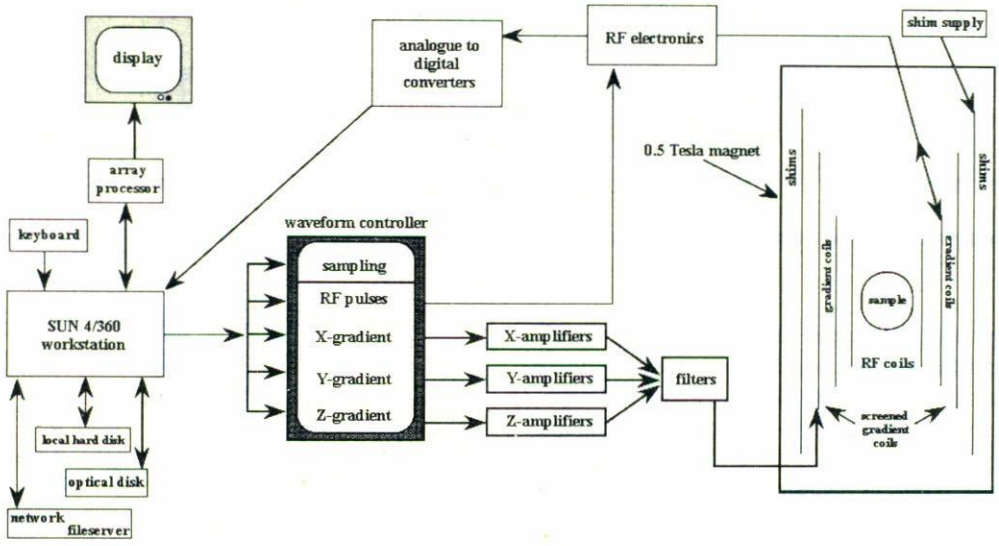

FIGURE 5. Block diagram of whole-body Echo-Planar Imaging system.

as in Fig. 5, an extra phase change happens producing $\beta = 0$ for the second echo. An echo is formed due the re-phasing of static spins at the end of each pair of pulse gradient, while the moving spins re-phase only after even numbers of bipolar pulses. This phenomenon is named the even-echo effect or flow compensation [161, 162].

Guilfoyle, *et al.* [77], Symms [124], Gibbs [125] and Rodriguez *et al.* [70] have demonstrated previously that the combination of EPI and a unipolar phase encoding sequence [160] can be used to measure flow. In the present work, the same flow encoding sequence shown in Fig. 4 precedes a Half-Fourier EPI experiment. The RF pulses of this sequence are non-selective. A spin-echo is formed by the static spins, after application of the 90° and 180° RF pulses. The second 90° pulse produces a realignment of the magnetization along z-axis when it is applied along the x-axis in the rotating frame while there is no effect when it is applied along the y-axis. The two gradient pulses produce no net phase accumulation for the stationary spins.

The combination of the first two RF pulses and gradients lobes, leads to an accumulation of phase, as described previously for flowing spins. The function of the second 90° pulse is to store either the $M_x = M_0 \sin\beta$ or the $M_y = M_0 \cos\beta$ component of the magnetization along the z-axis, for subsequent interrogation by the EPI experiment. In the cosine experiment, the magnetization is tipped back along z-axis by applying the second 90° pulse along the x-axis. To destroy any remaining transverse magnetization a spin phase scrambling gradient is employed, before the normal EPI experiment. The sine experiment is performed, by applying the second 90° pulse along the y-axis and the remaining signal is exterminated in the same way as in the cosine experiment. EPI is then able in two experiments, to produce images depicting cosine and sine of β. A schematic description of this sequence is shown in Fig. 4. The sine image allows direct visualisation of the flowing spins, since the static spins are suppressed. Such images are similar to time-of-flight angiograms. The cosine image offers a bright image of the static structures as well as some flow-encoded information. It is necessary to have both components to obtain qualitative flow information. This information can be gained with the following analysis.

Assuming that for a particular pixel the signal in the sine and cosine images is given by A and B, respectively,

$$A = S_0 \sin\beta, \tag{2}$$

$$B = S_0 \cos\beta, \tag{3}$$

where S_0 is the signal from the Half-Fourier EPI experiment. To establish an expression for the velocity of spins, Eq. (2) and Eq. (3) are divided to cancel the term S_0, and substituting for b from Eq. (1), the velocity can be expressed as

$$v = \frac{\tan(A/B)}{\gamma G_x(\tau^2 + \tau t)}. \tag{4}$$

One advantage of this method is that no calibration experiment is needed, since the term S_0 has been removed. The measured velocity, v, is the component in the direction of the flow encoding gradient.

2.3. Flow artefacts in echo-planar imaging

Motion produced by flow, as found in the great arteries, affects significantly the reconstructed MR image. Translation motion of tissue, as the motion of the chest wall during breathing, is another good example of this type of movement. If an object moves during acquisition of the data (flow or translational), the image will blurred: these unexpected and even bothersome are called *artefact.* However, artefacts may end up opening new doors and even new directions in research within MRI. Most of motion artefacts are due to a combination of flow and translational motion.

We used different techniques to eliminate them, although the two types of flow artefacts generate nonzero phase at the echo. For flow artefacts employing a gradient it is plausible to obtain a zero phase by carefully adjusting the gradient amplitude and timing along the flow direction. On the other hand, translational motion between RF pulses can be corrected by freezing the motion or collecting data when the tissue of interest is at one spatial location.

It is particularly relevant to study the effects MBEST imposes on spins in motion before any attempt is made to adapt EPI as a flow measurement sequence. EPI is insensitive to the time-of-flight phenomena outlined above. As long as spins stay within the volume of the gradient and RF coil linearity of 20 cm, for 128 ms which implies velocity magnitudes less than 1.6 m/sec, no effect of this type will take place. The selective excitation process last for 3.5 ms, and consequently only spins moving at speeds greater than 60 cm/sec will transverse the sensitive slice in this time and thus not be properly excited.

EPI regularly suffers from ghosting and blurring artefacts, geometric distortion and signal loss. This is occasioned by echo miscentring, gradient amplitude errors, movement, eddy currents and timing errors. Ghosting in the phase encoding direction regularly degrades the image. These ghosts are the result of the phase differences between odd and even echoes. The disparity originates from the inexact timing of the readout gradients, temporal asymmetry of the analogue filter and static field inhomogeneities. It has been recently reported that the visibility of structure in cardiac EPI images changes during systole and diastole: respiration, cardiac motion and blood flow are responsible for this artefact [163]. Many groups have been working extensively on different approaches to reduce these artefacts [163–170].

If EPI is performed under conditions of saturation recovery, spins will experience the phenomena of spin refreshment. After several experiments static spins which remain in the slice become partially saturated whilst spins flowing into the slice from surrounding regions are fully relaxed and therefore give a stronger signal [125]. The sensitivity of EPI to flow phenomena, particularly at flow rates encountered within the human body can be advantageous. Since EPI is an ultra-fast imaging technique, it is well suited to adaptation to flow measurements. The method can also be used in real-time angiography.

2.4. The half Fourier method

Whenever the four k-space quadrants are scanned, filling the whole of the space, this is designated as a full Fourier technique. The Fourier transform generates information containing real and imaginary parts with a well-defined phase. Taking the modulus of the two parts, give rise to modulus images in which all phase effects are removed. However, these methods can require long imaging times.

To abbreviate the long imaging times of the full Fourier methods [77], we can scan only half of the k-space [125, 171] and then reconstruct the other half using the Hermitian symmetry property of the Fourier transform of the NMR signal, $S(-k) = S^*(k)$ [172]. Then, in some cases only half the number of the experiments are essential. Nevertheless, this method demands zero filling before Fourier transformation. Filtering is needed to avoid ringing at the edges produced by the truncating step function. Phase variation causes problems since the Hermitian symmetry is lost. Such phase variation results from T^2 decay, misalignment of the signal detection and gradient eddy currents. These problems can be overcome by using another type of partial sampling scheme which makes use of slightly more than half of the k-space data in one encoding direction [171]. This enables us to construct a coarse phase map from the symmetric data around the origin, which will be employed afterwards to correct the phase errors.

This technique uses approximately half of the data lines filling k-space, without any reduction in resolution [138, 139]. It makes use of a phase correction procedure in the image domain. For example, an 128×128 image is formed with 72 echoes in 70 ms. A coarse phase map will be constructed using the central 16 echoes, which subsequently will be used in phase correction [173, 174]. There are others half Fourier methods to reduce the image acquisition in EPI [77–79] as well other imaging methods leading to reduce the acquisition time [175–178].

3. Overview of the EPI imager

The 0.5 T imaging system employed to carry out all the flow experiments, is outlined in this section. The author was not involved with the design or installation of the system. The present imaging system is the result of many years of work done by a number of people, who have written the software and designed and fabricated the hardware in-house, with some commercial hardware being built to specification. Figure 5, shows a schematic description of the 0.5 T Nottingham system developed specifically to perform echo-planar imaging.

3.1. The magnet

This imaging system is based around a superconducting magnet manufactured by Oxford magnet technology [179], with a magnetic field strength of 0.52 Tesla, which generates a Larmor frequency of 22.03 MHz (proton resonance frequency). It has a horizontal inner bore of 92 cm and a shim set (13 resistive coils) to compensate the field distortions caused by site problems and fabrication defects. The shim is able to produce a field homogeneity of 3 p.p.m. within a 30 cm diameter central sphere. To screen out the RF noise, the magnet ends are surrounded by an earthed Faraday cage of aluminium mesh.

3.2. The gradients coils

Three actively screened whole-body gradient coils are use to generate the three orthogonal linear field gradients (transver-

TABLE I. Summary of gradient system specifications for a 0.5 Tesla whole-body system. (Oxford superconducting magnet—manufactured in 1986)

Gradient	x	y	z
Usual Operation	Read	Broadening	Slice select
Parallel Inductance [μH]	97	97	92
Efficiency [$mTm^{-1}A^{-1}$] (parallel)/(series)	0.031/0.062	0.032/0.064	0.047/0.094
Maximum Current [A/pair]	120	120	120
Maximum Voltage [V]	320	320	320
Resistance [Ω]	0.03	0.03	0.03
Number of Pairs Amplifiers	4	3	1
Driving Mode	current	current	current

se x and y, and slice selection, z). EPI requires the use of large and rapidly switched magnetic field gradients. Such gradients produce undesired eddy currents in the metallic structures of the magnet body. Thus, secondary coils of opposite polarity, surrounding the corresponding gradient coils, were used to prevent the formation of eddy currents. The gradient coils have inner diameters of 60 cm. The power required by the gradients is supplied by Techron 7790 (3 phase, 415 V) linear power amplifiers, all wired as push-pull pairs. A current of 120 A at a peak voltage of 320 V is provided by each pair. The gradients are driven in current mode to ensure accurate following of the input gradient waveform demands. Usually, the gradient coils needed a rise time of 400 μs to reach their maximum amplitude. This parameter determines the gradient change per unit time or slew rate, which in turn, is dependent on the coil inductance and amplifier voltage. Another important parameter is the duty cycle of the amplifier, which characterises the proportion of the time that the amplifiers are on driving a particular pulse sequence. A standard EPI experiment, whose duration is 128 ms, produces a duty cycle of around 26%, when repeated 8 times in 4 seconds. The specifications of the gradient coils are summarised in Table I.

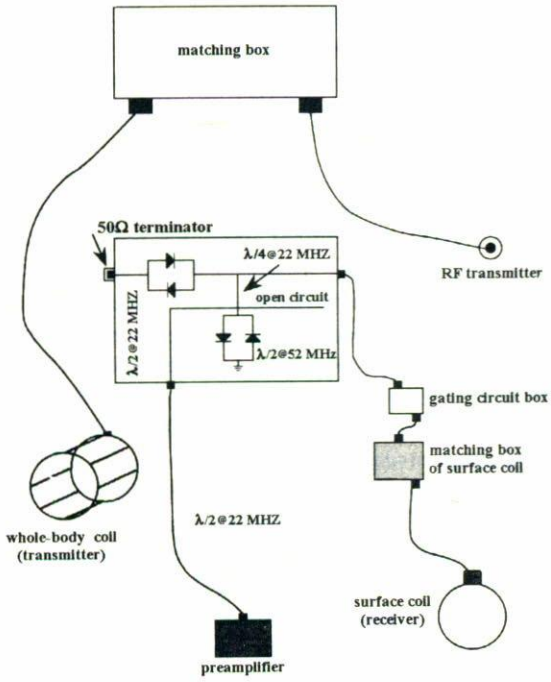

FIGURE 6. Diagram of dual coil system.

3.3. The radio frequency coils

Two RF coils were used in all the flow experiments, since this two-coil mode allows the receiver and transmitter to be optimised individually. The transmission coil was a RF whole-body coil [180–193] built by Dr. M. Symms and optimised by Dr. P. Boulby. This coil has a length of 50 cm and an inner diameter of 50 cm. The coil surrounded by a slotted screen which avoids coupling with external conductors, whilst minimising the generation of eddy currents when switching the gradients. This bird-cage coil [180–184] was tuned to resonate at 22.03 MHz. The quality factor (Q) is around 50 when the coil is loaded with a volunteer or a water phantom. The coil is matched to 50 Ω with a matching system consisting of an inductive-capacitive π-network. The two-coil array is illustrated in Fig. 6. The reception coil was a surface coil [194–196] designed and fabricated by Dr. P. Tokarczuk and optimised by myself (see Fig. 7a). The surface coil has has circular shape and is 24 cm in diameter. The Q value of the cardiac coil is approximately 34 when loaded on a volunteer. The coil was matched to 50 Ω with a specially designed matching box. A circuit diagram is shown in Fig. 7b. In order to reduce the coupling between the whole-body coil and the cardiac coil, as well as protecting the surface coil, a gating circuit was implemented (see Fig. 8). During RF transmission, a DC control voltage is applied to the gating circuit and the PIN diode switches on thus de-tuning the surface coil, so protecting it from the pulse from the whole-body transmitter and avoiding coupling between the two coils. Further protection of the preamplifiers is provided by the crossed-diodes and l/4 line shown in Fig. 9. When the diodes are biased on, an open circuit is seen at point A, thus protecting the pre-amplifier during transmission. In single coil operation the transmitter amplifier is connected in place of the 50 Ω load. The l/4 @ 52 MHz cable acts as a band-stop filter to RF at 52 MHz (the upper-side-band frequency).

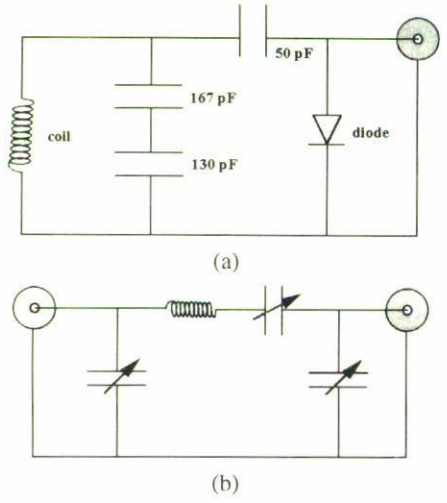

FIGURE 7. a) Circuit of cardiac coil, b) Matching circuit of cardiac coil.

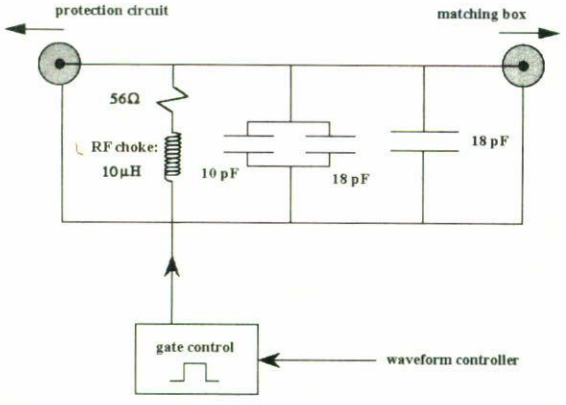

FIGURE 8. Diagram of gating circuit. The capacitors in this circuit are part of the tuning circuit.

3.4. The radio frequency electronics

The principles of standard heterodyne transmission and reception form the basis of the RF electronics. The carrier frequency is generated by a frequency synthesizer (Wavetek 5130A), operating 15 MHz above the frequency required (22 MHz). The carrier is fed to the RF modulator along with the pulse shape information from the RF channel of the waveform generator. Here is mixed with the 15 MHz reference frequency to form a RF pulse at the desired frequency. The pulse is amplified by a 2 kW power amplifier (Eddystone Radio H1301). Since the FID signal produced is the order of μV, a preamplifier of high gain and low noise (Trontech W100F 50 dB gain) was used to increase the signal to the order of mV. This amplifier is placed within the shield of the imaging system, so the effect of attenuation in the connecting cable is minimized.

After further amplification the signal is demodulated to a frequency in the range of kHz by mixing it with a reference signal (heterodyning), and then filtered using a low-pass filter. Finally, it is split into its real and imaginary parts by quadrature phase sensitive detection before it is sampled by the ADC's (analogue-to-digital converters). The signal is digitised with a dual 16 bit Hytek ADC whose maximum sampling rate is 10^6 complex samples per second. Then, it is stored in the workstation's short-term memory (SUN computer), before it is Fourier transformed. This protection circuitry is also used in single coil mode.

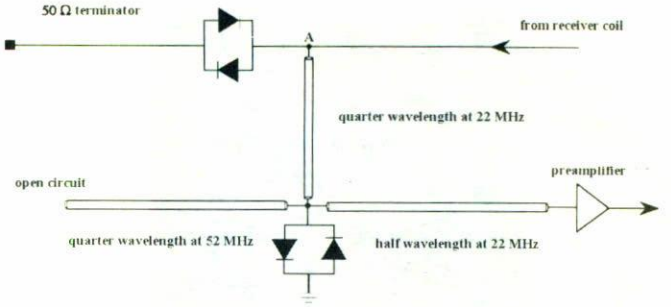

FIGURE 9. Protection circuit.

3.5. The computing systems

The experiments were controlled with a SUN4 workstation which was interfaced to a waveform controller designed by Dr. P. Glover [hardware] and Dr. R. Coxon [software]. The waveform controller manipulates the imaging parameters on screen in real time. It is possible to develop simple and flexible sequences with a gradient and RF channel time resolution of 1 μs and sampling channel resolution 1/16 μs. An AT&T pixel machine was used to perform the Fast Fourier Transformation: this array processor is able to produce 128 $\times$ 128 (or 128 $\times$ 64) images up to a rate of 10 frames per second. A high-resolution monitor was used to display the image data. Afterwards, images can be accessed from a console via a network for processing if required. Image data can be stored on a local hard disk whose memory size is 350 MB and then transferred to magnetic tapes or optical disks.

4. Experiment and method

The present flow sequence is based on a Full-Fourier EPI scheme developed previously in Nottingham [77, 124], a detailed description of the original work can be found in [125]. The sequence was implemented on a 0.5 T imager, described above.

Transaxial 128 $\times$ 128 images, with a slice of 1 cm thickness and 2.5 mm in-plane resolution were generated. Two coils were employed: a surface coil was used as a receiver and a whole-body coil as a transmitter. To avoid coupling between the 2 coils, a gating circuit was introduced into the system. Before the flow experiment was set up, the flow sequence was calibrated by producing HF-EPI images with a water reservoir and a pipe phantom.

The first phantom contained static water and the second consisted of a pipe bent to form an U shape so that two oppo-

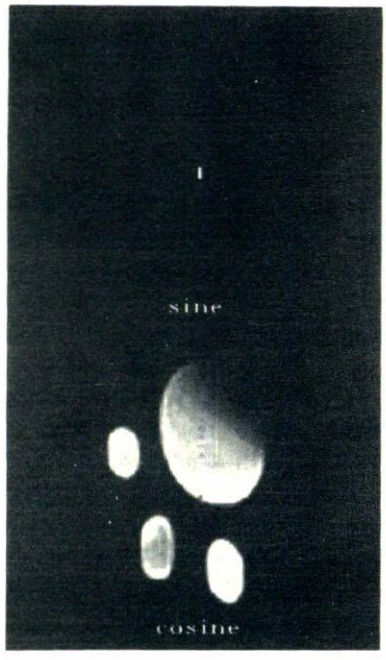

FIGURE 10. Phantom images of stationary water using Flow Encoded Half-Fourier EPI. A) sine or weak omponent and b) cosine or strong component.

site flow directions could be determined. The water reservoir was placed on top of the pipe and then the pipe was installed through the length of the scanner. A surface coil was placed on top of the water phantoms. Thus, in the image, three circles appeared: two carried flowing water and one with stationary water. The third one was used as an indicator to differentiate between the sine and cosine images in the dynamic situation. In order to have static water in the pipe as well, it was filled with water from a tap. Thereafter, the strength (G), duration (t) and delay time (τ) of the flow pulses, were varied until the sine image was sufficiently nulled and the cosine signal was maximum. Calibration images are shown in Fig. 10. The corresponding values are $t = 11$ ms, $\tau = 1.2$ ms, $G = 0.6$ mT/m. Although Eddy currents were present, their effects were sufficiently cancelled by adjusting the delay time τ, (see Fig. 2).

A critical parameter in HF-EPI acquisition is the strength of the flow encoding gradient, G. This gradient controls the amount of phase shift produced by a given velocity. An alternate and commonly used parameterization is to report the velocity that produces a phase shift of $\pi/2$ [Eq. (4)]. This parameter is referred to as the encoding velocity V_{enc}. To compute the encoding velocity for this particular experiment, the variables τ, t, G and γ were taken as above, giving an encoding velocity of around 70 cm/sec. This provided us with a good interval of velocities in performing our flow experiment.

Another experiment was performed to assess the reliability of the gradient strength. The calibration procedure was repeated on a bottle of 12 cm diameter, varying G. The times

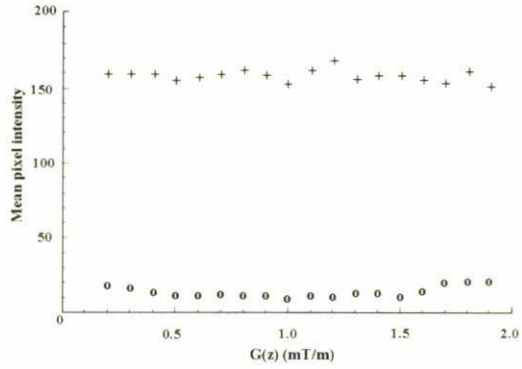

FIGURE 11. Graph showing the range of the gradient strength in which the degree of the separation of the two channels remains adequate to obtain a good calibration. (+) sine component and (o) cosine component.

τ(1.2 ms), t(11.2 ms) and the duration time of the non-selective RF pulses were kept constant throughout the experiment. The average of the signal intensity in both components was estimated using a MATLAB program, which essentially masked out the images to produce a ROI, then the mean of the pixels was computed. The plot of Fig. 11 indicates the region of G within which, Half-Fourier EPI flow imaging can be satisfactorily performed using this particular imaging system.

The flow experiment was performed by supplying water through the pipe from a water tap, so various flow rates were produced. A long inlet length was provided to ensure laminar behaviour in the imaging region. Images for each component were acquired for different flow rates. Two images with the intensity of the images weighted by the sine or cosine of the phase were generated. Each experiment was repeated 5 times to assess the reproducibility of the velocity measurement. For comparison, the velocity of water flow was measured independently from the MR imaging by timing the collected volume by the bucket and stopwatch technique. The following expression was used to compute the water velocity: $Q = VA$, where Q is the flow rate, V is the average water velocity and A is the cross-sectional area of the pipe with a diameter of 2 cm. The diameter of the tube in the image is approximately 12 pixels. Thus, it is valid to associate a unique velocity with each individual pixel.

5. Results

In order to calculate the velocities from the flow encoded images it is necessary to establish a method of calculation. The MRI signal intensity [77] integrated over the pipe cross section is

$$s = \int_0^R 2\pi r \rho(r) \exp(i\kappa V)\, dr, \tag{5}$$

where,$\rho(r)$ is the fluid density here taken as unity and the flow velocity at radius r, $V(r)$ is assumed to be laminar, $\kappa = \gamma G(\tau^2 + \tau t)$, and R is the pipe radius.

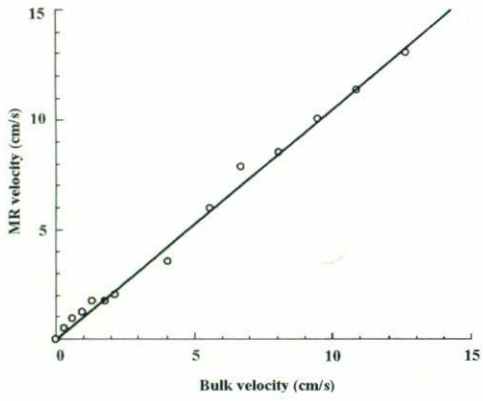

FIGURE 12. Plot illustrates the relationship between the bulk velocity and Half-Fourier EPI velocity measurements. The linear regression for this data is $V_{\mathrm{NMR}} = 1.06V_{\mathrm{Bulk}} + 0.062$ and $R^2 = 0.98$.

Assuming that the average velocity behaves in a laminar fashion, then the signal intensity is determined by [77]

$$s = \frac{R^2\pi}{kV_m}\left\{\sin\left(\kappa V_m\right) + i\left[1 - \cos\left(\kappa V_m\right)\right]\right\}. \qquad (6)$$

The two parts in Eq. (6) correspond to the sine and cosine experiments as described before. The direct measurement of the velocity can be gained with the division of these two components:

$$\tan\left(\frac{\kappa V_m}{2}\right) = \frac{1 - \cos\left(\kappa V_m\right)}{\sin\left(kV_m\right)}. \qquad (7)$$

From Eq. (7), V_{NMR} can be estimated by

$$\frac{\kappa V_m}{2} = \tan^{-1}\left(\frac{A}{B}\right) \qquad (8)$$

where A and B here represent the averages of the sine and cosine images, as in Eqs. (2) and (3).

We continued to measure the velocity in the pipe for the different flow values generated with the water tap. MATLAB and an expressly written C language program were used to calculate the NMR velocity. Images were masked out with a circle to separate the region of interest (ROI) from the rest of the image. Thus, interrogating the sine and cosine ROI with the software programmes, assuming [Eqs. (2) and (3)] that each pixel represents one velocity, it is possible to produce velocity maps for a particular flow rate. Flow maps are an excellent way to visualise the flow phenomenon in a pipe as well as in arteries.

The mean values were calculated by masking all the images and then calculating the mean of the pixels in the ROI. This approach presented some difficulties, since it was not straightforward to distinguish between the pipe wall and the background noise. At the perimeter of the ROI, some of the pixels include both image and noise, but, in the case of large ROIs, the inclusion of these pixels, does not greatly influence the measurements of the average velocity [39, 42]. In Fig. 12, the velocity in the pipe computed using the known flow rate

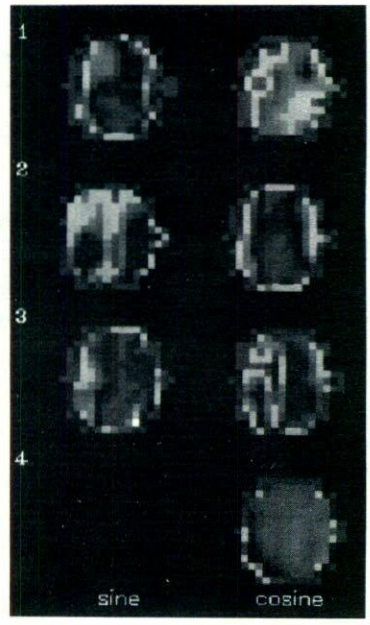

FIGURE 13. Images of the sine and cosine components of a water phantom 2.5 cm in diameter.

is compared against the average NMR velocity (V_{NMR}), calculated using Eq. (7) and the experimental data. This plot and linear regression of the data stress the excellent agreement of the NMR velocity with the actual velocity in the pipe. Thus, it can be implied that $V_m = V_{\mathrm{NMR}}$. This indicates a linear function over the flow range studied and confirms the laminar flow in the pipe. The sine and cosine experiments show a regular variation in the signal, see Fig. 13. The velocity maps of Fig. 14 exhibit the parabolic profiles expected from the analysis above. A more detailed analysis of the variation of the signal intensity of the two components of Eq. (6), has been reported by Guilfoyle [77].

The laminar condition in the pipe can be lost if the velocity reaches a critical point, normally at higher velocities. At this point the smooth flow cannot be preserved so the water flow becomes more sensitive to disturbances. The motion of the fluid turns irregular, random and turbulent. The Reynolds number, Re [162], offers a criterion to distinguish between laminar and turbulent flow. This dimensionless quantity in a circular pipe is expressed as

$$Re = \frac{Vd}{\nu}, \qquad (9)$$

where V is the average velocity, d is the pipe diameter and ν is the kinematic viscosity of water. According to McDonald [37] and others [38–41, 49, 52] a lower critical value of Re can be 2500 for water in a pipe. However, this is an empirical number and strongly depends upon the experimental conditions. To find out the critical points of this experiment, this value was replaced in Eq. (9) with a kinematic viscosity of $\nu = 1.002 \times 10^{-6}$ m^2/s at 20°C [197], producing a limiting velocity of 12 cm/s. Experimentally, slightly higher

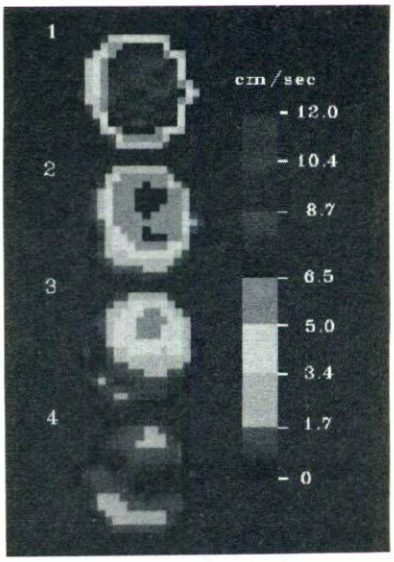

FIGURE 14. Velocity maps at lower velocities show a more predominant laminar behaviour. The velocity measurements were calculated at the following rates: 10.33 ml/s, 2) 1.25 ml/s, 3) 0.58 ml/s and 0.24 ml/s.

velocity could be to obtained before the flow was fully turbulent (see Fig. 13). Reynolds number predicts that at lower velocities the laminar behaviour is predominant as is illustrated in Fig 14. There is an excellent concordance between the V_m and V_{NMR} within this region. For completeness, the flow rate was increased until the turbulent region was reached. In the turbulent region, the smooth pattern is lost and a more chaotic behaviour starts to be predominant: velocity maps for this region were acquired and presented in Fig. 15.

6. Conclusions

It has been demonstrated that EPI flow imaging can be combined with a reduced data acquisition method and delay time,

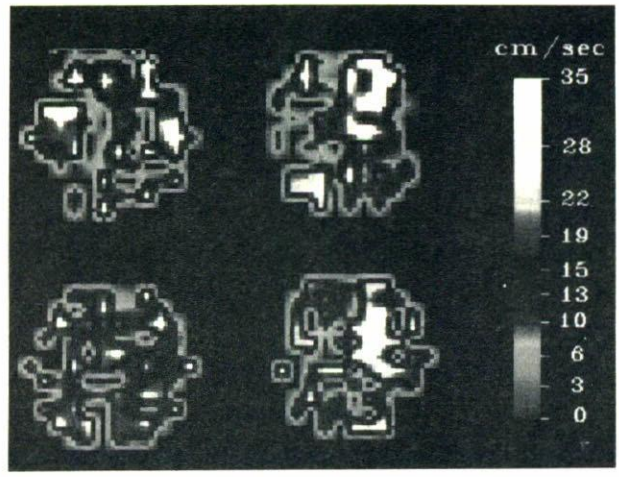

FIGURE 15. Velocity maps of a water phantom in the presence of turbulence. The typical behaviour of the laminar region is transformed into a chaotic one. The variation of the signal between velocity maps is erratic as well.

to provide a real-time technique for measuring flow in pipes. This scheme reveals the potential to obtain relevant flow information. This flow imaging technique compares very well with the previous flow sequence already established which use full-Fourier MBEST imaging module [77] and other ones validated by other groups [123]. It is important to highlight that delay time τ in the phase shift equation [Eq. (1)], proved to be a very useful tool to effectively eliminate Eddy currents. Flow measurements made in vitro with this technique have proved to be accurate. It offers a sound method to differentiate between laminar and turbulent flow from the analysis of velocity. Also, 2D velocity maps may offer a visualisation technique to study flow behaviour such as fully developed turbulent flows in pipes. These velocity maps may be combined with the wavelet analysis to produce a method able to investigate flow mechanics in both time and frequency simultaneously.

1. W.W. Bloch, F. Hansen, and M.E. Packard, *Phys. Rev.* **70** (1946) 127.
2. F. Bloch, *Phys. Rev.* **70** (1946) 460.
3. F. Bloch, W.W. Hansen, and M.E. Packard, *Phys. Rev.* **70** (1946) 474.
4. F. Bloch, *Nature* **118** (1953) 425.
5. F. Bloch, *Nature* **233** (1971) 374.
6. E.M. Purcell, H.C. Torrey, and R.V. Pound, *Phys. Rev.* **69** (1946) 37
7. E.M. Purcell, *Science* **118** (1953) 431.
8. N. Bloembergen, E.M. Purcell, and R.V. Pound, *Phys. Rev.* **73** (1948) 679.
9. E.L. Hahn, *J. Geophys. Res.* **65** (1960) 776.
10. E.L. Hahn, *Phys. Rev.* **80** (1950) 580.
11. G. Suryan, *Proc. Indian Acd. Sci.* **Sect. A. 33** (1951) 107.
12. A.I. Zhernovoi and G.D. Latyshev, *NMR in a Flowing Liquid* (Plenum, New York, 1965).
13. D.W. Jones and T.F. Child, *NMR in Flowing Systems*, Advances in Magnetic Resonance, Editions J.S. Waugh, (Academic Press, New York, 1976) Vol. 8.
14. J. Stepisnik, *Measuring and Imaging of Flow by NMR*, Progress in Nuclear Magnetic Spectroscopy, (Editions J.W. Emsley, J. Feeney, and L.H. Sutcliffe, (Pergamon, Oxford, 1985) Vol. 17.
15. C.L. Dumoulin, *Flow Imaging*, Medical Magnetic Resonance, Editions A. Primer, T. Budinger, A. Margulis, (Society of Magnetic Resonance in Medicine, Berkeley, 1988).
16. C. Caprihan and E. Fukushima, *Phys. Report*, **198** (1990) 195.

17. N.J. Pelc *et al.*, *Magn. Reson. Q.* **10** 3 (1994) 125.

18. J.R. Singer, "Blood Flow Measurements by NMR", in *Nuclear Magentic Resonance in Medicine*, (Editions L. Kaufam, L.E. Crooks, A.R. Margulis, (Igaku-Shoin, 1981).

19. W.G. Bradley, "Flow Phenomena", *Magnetic Resonance Imaging*, (Mosby Co., St. Louis, 1988).

20. E. Fukushima, *Annu. Rev. Fluid Mech.* **31** (1999) 95.

21. D.K. Ku, *Annu. Rev. Fluid. Mech.* **29** (1997) 399.

22. J.R. Singer, *Science* **130** (1959) 1652.

23. J.R. Singer, *J. Appl. Phys.* **31** (1960) 125.

24. O.C. Morse and J.R. Singer, *Science* **170** (1970) 440.

25. Y. Takeda, *Int. J. Series B. Flu. Ther. Eng.* **38** (1995) 8.

26. R. Willink and D.H. Evans, *Ultrasound Med. Biol.* **21** (1995) 203.

27. S.K. Alam and K.J. Parker, *Ultrasound Med. Biol.* **21** (1995) 657.

28. R.W. Gill, *Ultrasound Med. Biol.* **11** (1985) 625.

29. R. Haerten and J. Kim, *Ultraschall. Med.* **14** (1993) 225.

30. R.L. Powis, *Radiographics*, **14** (1994) 415.

31. A. Herment and P. Dumee, *Euro. J. Ultrasound* **1** (1994) 345.

32. J.C. Bamber and M. Tristam, "Diagnostic Ultrasound", in *The Physics of the Medical Imaging*, (IOP Publishing, Bristol, 1990).

33. P.N.T. Wells, *Phys. Med. Biol.* **39** (1994) 2113.

34. T.J.H. Essex and P.O. Byrne, *J. Biomed. Eng.* **13** (1991) 189.

35. C.G. Xie *et al.*, *IEEE Proc. Circ. Dev. Syst.* **141** (1994) 357.

36. B.H. Brown, A. Leathard, A. Sinton, F.J. McArdle, R.W.M. Smith, D.C. Barber, *Proc. of 13th Ann. Conf. of IEEE and EMBS*, **13** (1991) 307.

37. D.A. McDonald, *Blood Flow in Arteries*, 2nd Editions (Edward Arnold Publishers, London, 1974).

38. C.G. Caro, T.J. Pedeley, and R.C. Schroter, *The Mechanics of the Circulation*, (Oxford University Press, Oxford, 1978).

39. W.R. Milnor, *Hemodynamics*, 2nd Edition (Williams & Wilkins, Baltimore, 1982).

40. D.H. Bergel, *Cardiovascular Fluid Dynamics*, (The Waterfriars Press, London, 1972) Vol. I and II.

41. Y. Fung, *Biomechanics: motion, flow, stress, amd growth*, (Springer Verlarg, New York, 1990).

42. T.J. Pedley, *The Fluid Mechanics of Large Blood Vessels*, (Cambridge University Press, Cambridge, 1980).

43. H.M. Lieberstein, *Mathematical Physiology: Blood Flow and Electrically Active Cells*, Modern Analytic and Computanional Methods in Science and Mathematics, No. 40, (Elsevier, New York, 1973).

44. I. Mirsky, *Cardiac Mechanics: Physiological*, Clinical and Mathematical Considerations, (John Wiley and Sons, New York, 1974).

45. Ch. Peskin, *Mathematical Aspects of Heart Phisiology*, (Courant Institute of Mathematical Sciences, New York University, New York, 1975).

46. J. Lighthill, *Mathematical Biofluiddynanics*, Regional Conference Series in Applied Mathematics, (SIAM, Philadelphia, 1975).

47. U. Dinnar, *Cardiovascular Fluid Dynamics*, (Boca Raton, CRC, 1981).

48. F.C. Hoppensteadt, *Mathematical Apects of Physiology*, (American Mathematical Society, Providence, 1981).

49. L.A. González-Pinzón, Tesis de Maestría, FI-UNAM, México, 1984.

50. L. Glass, P. Hunter, and A. McCulluh, (Editors), *Theory of Heart: Biomechanics, Biophysics and Nonlinear Dynamics of CardiacFunction*, Institute of Nonlinear Science, (Springer Verlarg, New York, 1989).

51. J. Mazumdar, *An Introduction to Mathematical Physiology and Biology*, Australian Mathematical Society, Lecture Series 4, (Cambridge University Press, Cambridge, 1989).

52. J. Strackee and N. Westerhof, (Editors), *The Physics of Heart and Circulation*, (Institute of Physics Publising, Bristol, 1993).

53. L. Axel, *Am. J. Roentgeol.* **143** (1984) 1436.

54. P. van Dijk, *J. Comput. Assist. Tomogr.* **8** (1984) 429.

55. D.J. Bryant, J.A. Payne, D.N. Firmin, and D.B. Longmore, *J. Comput. Assist. Tomogr.* **8** (1984) 588.

56. T.W. Redpath, D.G. Norris, R.A. Jones, and J.M.S. Hutchison, *Phys. Med. Biol.* **29** (1984) 891.

57. D.A. Feinberg *et al.*, *Magn. Reson. Med.* **2** (1985) 555.

58. D.N. Firmin, G.L. Nayler, P.J. Kilner, and D.B. Longmore, *Magn. Reson. Med.* **14** (1990) 230.

59. A. Caprihan, S.A. Altobelli, and E. Benitez-Read, *Magn. Reson. Med.* **90** (1990) 71.

60. M. Singh and K. Oshio, *IEEE Trans. Nuc. Med.* **37** (1990) 1316.

61. S. Kanayama, S. Kuhara, and K. Satoh, *Proc. 3 rd Sci. Meeting Soc. Mang. Reson. Med.*, Nice, (1995) p. 746.

62. P.D. Gatehouse and D.N. Firmin, *Proc. 3 rd Sci. Meeting Soc. Mang. Reson. Med.*, Nice, (1995) p. 568.

63. Hu. Xiaoping and H.Le. Tuong, *Proc. 4 th Sci. Meeting Soc. Mang. Reson. Med.*, (New York, 1996) p. 116.

64. G. Kashmar, A. Ersahim, H.K. Lee, and O. Nalcioglu, *Proc. 4th Sci. Meeting Soc. Mang. Reson. Med.*, (New York, 1996) p. 1478.

65. Y. Ng *et al.*, *Proc. 4th Sci. Meeting Soc. Mang. Reson. Med.*, (New York, 1996) p. 1603.

66. D.G. Nishimura, P. Irarrazaval, and C.H. Meyer, *Magn. Reson. Med.* **33** (1995) 549.

67. Q.S. Xiang and M. Henkelman, *Magn. Reson. Med.* **29** (1993) 422.

68. M. Lauzon and B.K. Rutt, *Magn. Reson. Med.* **30** (1993) 438.

69. G.C. McKinnon, *Mag. Res. Med.* **31** (1994) 682.

70. A. Rodriguez, B. Issa, R. Bowtell, and P. Mansfield, *13th Ann. Meeting Eur. Soc. Magn. Reson. Med. & Biol.*, (Prague, 1996).

71. P.D. Gatehouse, D.N. Firmin, S. Collins, and D.B. Longmore, *Magn. Reson. Med.* **31** (1994) 504.

72. H. Fischer, F. Schmitt, H. Barfuss, and H. Bruder, Books of Abstracts, 7^{th} *Ann. Meeting Soc. Mang. Reson.*, San Francisco, 1988.
73. G.T. Luk Pat, J.M. Pauly, and D.G. Nishimura, *Proc. 3 rd Sci. Meeting Soc. Mang. Reson. Med.*, (Nice, 1995) p. 86.
74. J.M. Pauly, K. Butts, G.T. Luk Pat, and A. Macovski, *Proc. 3^{rd} Sci. Meeting Soc. Mang. Reson. Med.*, (Nice, 1995) p. 106.
75. W.H. Perman *et al.*, *J. Magn. Reson. Imaging* **11** (1993) 357.
76. J. Bittoun *et al.*, *Magn. Reson. Med.* **29** (1993) 674.
77. D.N. Guilfoyle, P. Gibbs, R.J. Ordidge, and P. Mansfield, *Magn. Reson. Med.* **18** (1991) 1.
78. J. Bittoun *et al.*, *Magn. Reson. Med.* **29** (1993) 674.
79. C.P. Davis, G.C. McKinnon, J.F. Debatin, G.K. von Schulthness, *Eur. Radiol.* **6** (1996) 297.
80. D.P. Madio and I.J. Lowe, *Magn. Reson. Med.* **34** (1995) 525.
81. J.D. Pearlman and R.R. Edelman, *Radiol. Clin. North. Am.* **32** (1994) 593.
82. T. Miyati *et al.*, *Radiographics* **16** (1996) 595.
83. G.K. von Schultness, C.P. Davis, J.F. Debatin, and G.C. McKinnon, *Radiologe* **35** (1995) 952.
84. N.S. Cohen and R.M. Weisskoff, *Mag. Reson. Imaging* **9** (1991) 1.
85. Q. Chen, K.W. Stock, P.V. Prasad, and H. Hatabu, *Eur. J. Radiol.* **29** (1999) 90.
86. L. Hoisington, R.A. Miller, and B. Vreibel, *Radiol. Technol.* **69** (1998) 351.
87. M.A. Sargent and K.J. Poskitt, *Pediatr. Radiol.* **27** (1997) 545.
88. H.T. Nielsen *et al.*, *Magn. Reson. Med.* **41** (1999) 591.
89. A.J. Freeman, P.A. Gowland, and P. Mansfield, *Magn. Reson. Imaging*, **16** (1998) 765.
90. D.P. Madio, H.M. Gach, and I.J. Lowe, *Magn. Reson. Med.* **39** (1998) 574.
91. S. Naganawa *et al.*, *Am. J. Neuroradiol* **19** (1998) 739.
92. T. Niendorf, *Magn. Reson. Med.* **41** (1999) 1189.
93. L. Zha and I.J. Lowe, *Magn. Reson. Med.* **33** (1995) 377.
94. O. Heid, M. Deimling, and W.J. Huk, *Magn. Reson. Med.* **33** (1995) 143.
95. D.P. Madio and I.J. Lowe, *Magn. Reson. Med.* **34** (1995) 525.
96. M. Reiser and S.C. Faber, *Eur. Radiol.* **7 S5** (1997) 166.
97. R.J. van der Geest and J.H. Reiber, *J. Magn, Reson, Imaging* **10** (1999) 602.
98. Y. Yamashita, Y. Tang, and M. Takahashi, *J. Magn. Reson. Imaging* **8** (1998) 367.
99. D. Chien and R.R. Edelman, *Magn. Reson. Q.* **7** (1991) 31.
100. W.A. Stringer, *Clin. Neurosci.* **4** (1997) 110.
101. Q. Long *et al* , *Crit Rev. Biomed. Eng.* **26** (1998) 227.
102. F. Boudghene *et al.*, *J. Radiol. (FRANCE)* **80** (1999) 1011.
103. D. Didier, *J. Radiol. (FRANCE)* **80** (1999) 1042.
104. P. Croisille and D. Revel, *J. Radiol.* **80** (1999) 1054.
105. H. Sakuma *et al.*, *Invest. Radiol.* **34** (1999) 503.
106. J. Rodenwaldt *et al.*, *Rofo. Fortschr. Geb. Rontgenstr. Neuen. Bildgeb. Verfahr.* **171** (1999) 100.
107. C. Davis *et al.*, *Radiology* **191** (1994) 691.
108. T. Pfluger *et al.*, *Am. J. Roentgenol.* **173** (1999) 103.
109. V. Bousson *et al.*, *Am. J. Roentgenol* **173** (1999) 139.
110. E.E. van der Wall and J. Bax, *J. Nucl. Cardiol.* **6** (1999) 462.
111. A. Okumura *et al.*, *Radiographics* **19** (1999) 973.
112. D.R. Thedens, P. Irarrazaval, T.S. Sachs, C. H. Meyer, D.G. Nishimura, *Magn. Reson. Med.* **41** (1999) 1170.
113. R.J. van Geuns *et al.*, *Coron. Artery. Dis.* **10** (1999) 261.
114. M. Busch *et al.*, *J. Magn. Reson. Imaging* **8** (1998) 944.
115. R.I. Pettigrew, J.N. Oshinski, G. Chatzimavroudis, and W.T. Dixon, *J. Magn. Reson. Imaging.* **10** (1999) 590.
116. S.B. Reeder, E. Atalar, A.Z. Faranesh, and E.R. McVeigh, *Magn. Reson. Med.* **41** (1999) 375.
117. W.R. Nitz *et al.*, *Radiologe* **39** (1999) 495.
118. N.L. Kelekis *et al.*, *Magn. Reson. Imaging* **17** (1999) 641.
119. J.E. Heiserman, *Neuroimaging Clin. N. Am.* **9** (1999) 253.
120. T.K. Foo, V.B. Ho, and P.L. Choyke, *Neuroimaging Clin. N. Am.* **9** (1999) 263.
121. H.E. Moller *et al.*, *Magn. Reson. Med.* **41** (1999) 1058.
122. M.P. Firmin *et al.*, *Magn. Reson. Med.* 12 (1989) 316.
123. J.F. Debatin *et al.*, *Magn. Reson Imaging.* **5** (1995) 656.
124. M.R. Symms, Ph.D. Thesis, The University of Nottingham, 1991, England.
125. P. Gibbs, Ph.D. Thesis, The University of Nottingham, 1990, England
126. P. Mansfield and P.K. Grannell, *J. Phys.* **C6** (1973) L422,.
127. P. Mansfield and A.A. Maudsley, *J. Phys. C: Solid State Phys.* **9** (1976) L409.
128. P. Mansfield and A.A. Maudsley, *J. Mag. Reson.* **27** (1977) 101.
129. P. Mansfield, *J. Phys. C: Solid State Phys.* **10** (1977) L55.
130. R. Ordidge, Ph.D. Thesis, The University of Nottingham, 1981.
131. S. Ljunggren, *J. Magn. Reson.* **54** (1983) 338.
132. A.M. Howseman *et al.*, *Brit. J. Rad.* **61** (1988) 822.
133. B. Chapman *et al.*, Magn. Reson. Med. **5** (1987) 246 .
134. M.K. Stehling, R. Ordidge, R. Coxon, and P. Mansfield, *Magn. Reson. Med.* **13** (1990) 514.
135. I.L. Pykett and R.R. Rzedizan, *Magn. Reson. Med.* **5** (1987) 563.
136. A.N. Garroway, P.K. Grannell, and P. Mansfield, *J. Phys.* **C7** (1974) L457.
137. P. Mansfield, P.G. Morris, and R. Ordidge, *Brit. J. Radiol.* **52** (1979) 242.
138. P.C. Lauterbur, *Nature* **242** (1973) 190.
139. R. Damadian, *Science* **171** (1971)1151.
140. R. Damadian, U.S. Pat. 3 789 832, 17 March 1972.

141. P. Mansfield, *J. Phys. E: Sci. Instrum.* **21** (1988) 18.

142. I.L. Pykett, *Scientific American* **246** (1982) 78.

143. W.S. Hinshaw and A.H. Lent, *Proc. IEEE* **71** (1983) 338.

144. A. Kumar, D. Welti, and R.R. Ernst, *J. Magn. Reson.* **18** (1975) 69.

145. N. Bloembergen, *Nuclear Magnetic Relaxation*, (W.A. Benjamin, New York, 1961).

146. A. Abragam, *Principles of Nuclear Magnetism*, (Clarendon Press, Oxford, 1989).

147. C.P. Slichter, *Principles of Magnetic Resonance*, 3rd Edition (Springer-Verlag, Berlin, 1992).

148. E.R. Andrew, *Nuclear Magnetic Resonance*, (Cambridge University Press, London, 1969).

149. P. Mansfield and P.G. Morris, *NMR Imaging in Biomedicine*, (Academic Press, New York, 1982).

150. P.G. Morris, *Nuclear Magnetic Imaging in Medicine and Biology*, (Clarendon Press, Oxford, 1986).

151. C.N. Chen and D.I. Hoult, *Biomedical Magnetic Resonance Technology*, (Adam Hilger, IOP Publishing, Britain, 1989).

152. P.T. Callaghan, *Principles of Nuclear Magnetic Resonance Microscopy*, (Oxford University Press, Oxford, 1991).

153. J.W. Hennel and J. Klinowsky, *Fundamentals of Nuclear Magnetic Resonance*, (Longman Scientific and Technical, Essex, 1993).

154. S.R. Thomas and R.L. Dixon, (Editors), *NMR in Medicine, Instrumentation and Clinical Applications*, (AAPM, New York, 1986).

155. P. Sprawls, (Editor), *The Physics of MRI*, (American Institute of Physics, New York, 1993).

156. F.A. Rushworth and D.P. Tunstall, *Nuclear Magnetic Resonance*, (Gordon and Breach, New York, 1973).

157. J.T. Bushberg, J.A. Seibert, E.M. Leidholdt, and J.M. Boone, *The Essential Physics of Medical Imaging*, (Williams & Wilkins, Baltimore, 1994).

158. M.A. Foster and J.M.S. Hutchinson, (Editors), *Practical NMR Imaging*, (IRL Press, Oxford, 1987).

159. P.R. Moran, *J. Mag. Reson. Imaging* **1** (1992) 197.

160. E.O. Stejskal and T.E. Tanner, *J. Chem. Phys.* **42** (1965) 288.

161. H.Y. Carr and E.M. Purcell, *Phys. Rev.* **94** (1954) 630.

162. V. Waluch and W.G. Bradley, *J. Comput. Assist. Tomogr.* **8** (1984) 594.

163. S. Kanayama, S. Kuhara, and K. Satoh, *Proc. 3rd Sci. Meeting Soc. Mang. Reson. Med.* (Nice, 1995) p. 746.

164. P.D. Gatehouse and D.N. Firmin, *Proc. 3rd Sci. Meeting Soc. Mang. Reson. Med.* (Nice, 1995) p. 568.

165. Hu. Xiaoping and H.Le. Tuong, *Proc. 4th Sci. Meeting Soc. Mang. Reson. Med.* (New York, 1996) p. 116.

166. G. Kashmar, A. Ersahim, H.K. Lee, and O. Nalcioglu, *Proc. 4th Sci. Meeting Soc. Mang. Reson. Med.* (New York, 1996) p. 1478.

167. Y. Ng *et al.*, *Proc. 4th Sci. Meeting Soc. Mang. Reson. Med.* (New York, 1996) p. 1603.

168. D.G. Nishimura, P. Irarrazaval, and C.H. Meyer, *Magn. Reson. Med.* **33** (1995) 549.

169. Q.S. Xiang and M. Henkelman, *Magn. Reson. Med.* **29** (1993) 422.

170. M. Lauzon and B.K. Rutt, *Magn. Reson. Med.* **30** (1993) 438.

171. H. Fischer, F. Schmitt, H. Barfuss, and H. Bruder, Books of Asbtracts, *7th Ann. Meet. Soc. Mag. Res.*, San Francisco, 1988.

172. L.E. Crooks *et al.*, *Books of Abstracts, 5th Ann. Meet. Meet. Soc. Mag. Res.*, Quebec, 1986.

173. P. Margosian, *Books of Abstratcs, 4th Ann. Meet. Meet. Soc. Mag. Res.*, London, 1985.

174. P. Margosian, F. Schmitt, and D.E. Purdy, *Health Care Instru.* **1** (1986) 195.

175. A. Haase *et al.*, *J. Magn. Reson.* **67** (1986) 258.

176. A.M. Howseman *et al.*, *E. Brit. J. Rad.* **61** (1988) 822.

177. B. Chapman *et al.*, *Magn. Reson. Med.* **5** (1987) 246.

178. M.K. Stehling, R.J. Ordidge, R. Coxon, and P. Mansfield, *Magn. Reson. Med.* **13** (1990) 514.

179. Oxford Magnet Technology, *Manual for the* 0.3–2.0 *Tesla Whole Body Imaging Magnets*, (Oxford, 1982).

180. C.E. Hayes *et al.*, *J. Magn. Reson.* **63** (1985) 622.

181. C.E. Hayes, US Patent, **4 694 255**, 1987.

182. C.E. Hayes, US Patent, **4 692 705**, 1987.

183. C.E. Hayes and M.G. Eash, US Patent, **4 642 569**, 1987.

184. W.A. Edelstein, J.F. Schenck, O.M. Mueller, and C.E. Hayes, US Patent, **4 680 548**, 1987.

185. M.D. Harpen, *J. Magn. Reson.* **29** (1993) 263.

186. M.D. Harpen, *J. Magn. Reson.* **94** (1991) 550.

187. M.D. Harpen, *Med. Phys.* **17** (1990) 686.

188. J. Tropp, *J. Magn. Reson.* **82** (1989) 51.

189. J. Tropp, *J. Magn. Reson.* **95** (1991) 235.

190. D.I. Hoult and P.C. Lauterbur, *J. Magn. Reson.* **34** (1979) 425.

191. D.I. Hoult, *J. Magn. Reson.* **42** (1979) 42.

192. P.M. Joseph and D. Lu, *IEEE Trans. Med. Imaging* **8** (1989) 286.

193. T. Vullo *et al.*, *J. Magn. Reson.* **24** (1992) 243.

194. W.T. Sobol, *Rev. Magn. Reson. Med.* **1** (1986) 181.

195. Z.A. Fayad, T.J. Connick, L. Axel, *Magn. Reson. Med.* **34** (1995) 186.

196. C.D. Constantinides *et al.*, *Magn. Reson. Med.* **34** (1995) 92.

197. B.R. Munson, D.F. Young, T.H. Okiishi, *Fundamentals of Fluid Mechanics*, 2nd Edition (John Wiley & Sons, New York, 1994).

198. A. Rodriguez-Gonzalez, Ph. D. Thesis, The University of Nottingham, 1997, England.